Full length article

Experimental demonstration of a silicon-slot quasi-bound state in the continuum in near-infrared all-dielectric metasurfaces

J.F. Algorri [a,b,c], F. Dell'Olio [d], Y. Ding [e,f], F. Labbé [f], V. Dmitriev [g], J.M. López-Higuera [a,b,c], J.M. Sánchez-Pena [h], L.C. Andreani [i], M. Galli [i], D.C. Zografopoulos [j,*]

[a] *Photonics Engineering Group, University of Cantabria, Santander, 39005, Spain*
[b] *CIBER-bbn, Instituto de Salud Carlos III, Madrid, 28029, Spain*
[c] *Instituto de Investigación Sanitaria Valdecilla (IDIVAL), Santander, 39011, Spain*
[d] *Department of Electrical and Information Engineering, Polytecnic University of Bari, Bari, 70125, Italy*
[e] *SiPhotonIC ApS, Virum Stationsvej 207, Virum, 2830, Denmark*
[f] *Department of Electrical and Photonics Engineering, Technical University of Denmark, Ørsteds Plads, Bygning 343, Kongens Lyngby, 2800, Denmark*
[g] *Electrical Engineering Department, Federal University of Pará, PO Box 8619, Agencia UFPA, Belém, 66075-900, Brazil*
[h] *Department of Electronic Technology, Carlos III University, Madrid, 28911, Spain*
[i] *Dipartimento di Fisica, Università di Pavia, Pavia, 27100, Italy*
[j] *Consiglio Nazionale delle Ricerche, Istituto per la Microelettronica e Microsistemi, Via del fosso del cavaliere 100, Rome, 00133, Italy*

ARTICLE INFO

ABSTRACT

We theoretically and experimentally investigate a metasurface supporting a silicon-slot quasi-bound state in the continuum (qBIC) mode resonating in the near-infrared spectrum. The metasurface is composed of circular slots etched in a silicon layer on a sapphire substrate. The symmetry of the metasurface unit cell is reduced in order to provide access to the symmetry-protected mode, whose properties are investigated by finite-element full-wave and eigenfrequency analysis. The measured transmittance spectra verify the excitation of the investigated qBIC mode with experimental quality factors exceeding 700. The near-field distribution of the resonant qBIC mode shows strong field confinement in the slots, leading to high sensitivity values for refractometry.

1. Introduction

In recent years, bound states in the continuum (BIC) have developed into a new paradigm for trapping and confining resonant optical modes in photonic systems. In theory, pure BICs are dark states with infinite radiative lifetime in lossless systems with infinite structure [1] or permittivity approaching zero [2,3]. However, under realistic conditions, such as the finite extent of structures and material absorption, BIC manifest as Fano resonances with finite radiative and non-radiative quality factor (Q-factor) in what is termed as quasi-BIC (qBIC). Since their first theoretical [4] and experimental [5] demonstration in photonic systems, several works have investigated the underlying physics following theoretical frameworks [6].

Beyond the study of their fundamental physics, BIC have been increasingly applied in numerous breakthrough applications driven by advanced nanofabrication techniques [7]. The existence of optical BIC modes can be classified as symmetry-protected BIC (SP-BIC) [8], owing to symmetry-forbidden out-coupling, accidental or Friedrich–Wintgen BIC [9], as the outcome of radiation suppression of all open

channels, and Fabry–Perot BIC (FP-BIC) [10]. Various photonic systems can support this diversity of BIC types [11]. Indeed, they have been thus far demonstrated in numerous geometrical configurations, including gratings [12], waveguides [13], photonic crystals [14] and metasurfaces [15].

Among these options, BIC-resonant metasurfaces are being extensively researched. Metasurfaces are two-dimensional arrangements of subwavelength optical scatterers capable of drastically modifying impinging wavefronts. In the case of dielectric metasurfaces, high-permittivity scatterers exhibit a variety of Mie resonances that allow for both electric and magnetic responses even at optical frequencies. For instance, the interaction among dipole resonances (namely, electric dipole, ED, magnetic dipole, MD, and toroidal dipole, TD) offers several possibilities, e.g., Huygens' metasurfaces (interference of orthogonal ED and MD) [16], Janus dipole (interference of $\pi/2$ phase-shifted ED and MD) [17], and anapole states (interference of ED and TD) [18]. Being no exception, BIC modes too can be studied in terms of their multipole fingerprint, by employing appropriate tools such as the multipole

---

* Corresponding author.
E-mail address: dimitrios.zografopoulos@artov.imm.cnr.it (D.C. Zografopoulos).

decomposition technique, which has been used to investigate both SP-BIC and FW-BIC [6,19], as well as qBIC in dielectric nanoresonators by coupling Mie resonances with FP cavity-like modes [20]. In a previous work, we proposed and investigated a SP-BIC resonating at telecom near-infrared (NIR) wavelengths in metasurfaces based on split ring ultrathin slots etched in silicon [21]. Although the metasurface investigated in this work belongs to the type introduced in [21], the presented study is fundamentally different as: (i) it regards the properties of a qBIC resonant mode of different symmetry, not studied in [21], (ii) it focuses on the refractometric performance of the proposed qBIC resonant metasurface, and, most important, (iii) it provides the first experimental results on split-ring silicon metasurfaces.

In particular, we theoretically and experimentally demonstrate a SP-BIC with very strong field confinement in circular slots defined by electron-beam lithography (EBL) and fabricated via inductively coupled plasma (ICP) etching on a silicon-on-sapphire metasurface. First, the SP nature of the BIC silicon-slot mode is demonstrated through an eigenfrequency study, symmetry-analysis considerations and full-wave light propagation simulations. It is shown that the radiative Q-factor of the resonance can be adjusted by controlling the degree of asymmetry in the metasurface unit cell, which is introduced by reducing the arc length of one of the two constituent circular slots. Thanks to the almost total electric field confinement in the slots, the NIR resonant wavelength of the qBIC mode shows strong dependence on the refractive index of the surrounding material, with sensitivity equal to 435 nm/RIU in the case of gas sensing.

The existence of the investigated silicon-slot qBIC mode is experimentally verified by measuring the transmission spectra of a set of fabricated samples with different degrees of asymmetry. The measured spectra confirm the trend in the variation of the qBIC mode resonant wavelength as a function of the asymmetry. Q-factors as high as 725 are measured and the possible factors leading to the observed resonance broadening are thoroughly discussed. This experimental proof-of-concept demonstration of a NIR-qBIC in silicon-on-sapphire metasurfaces introduces a new paradigm for the development of IR refractometric sensors or other devices based on enhanced light–matter interaction thanks to strong optical field confinement in deeply-subwavelength resonant cavities.

2. Design and theoretical analysis

The layout of the investigated MS is presented in Fig. 1(a). A periodic array of circular slot segments is etched in a thin silicon layer on a sapphire substrate. The incident planewave is y-polarized and it impinges perpendicularly on the MS. The MS unit cell, shown in Fig. 1(b), is composed of two segments of a circular slot ring (CSR) with inner diameter w and slot width s. The distance between adjacent CSR is g and, therefore, the MS pitch equals $p = w + g + 2s$. The CSR is interrupted by two symmetrical silicon bridges of width d, which reduces the 2D symmetry of the unit cell from C_{4v} to C_{2v} (in Schoenflies notation [22]). Then, the length of one of the two slot segments is reduced by introducing the asymmetry parameter d_x, which asymmetrically increases the width of the silicon bridge, and lowers the symmetry of the structure to C_s. This symmetry reduction is necessary for the excitation of the investigated symmetry-protected qBIC resonant mode, as it will be further discussed. It is remarked that, although the introduction of the silicon gap d is not sufficient to allow excitation of the target BIC mode, it facilitates the fabrication of the asymmetric samples ($d_x \neq 0$), which is done by increasing the width of the existing silicon bridge. On the contrary, a single bridge of width d_x in the range of few nanometers would pose serious fabrication challenges due to EBL resolution limitations.

Fig. 1(c) and (d) show the scanning electron microscope (SEM) images for two of the samples characterized by $d_x = 0$ and $d_x = 80$ nm, respectively. All samples were fabricated following a standard EBL nanofabrication protocol (details in Section 3). The design values for

the geometrical parameters of the MS are: $s = 40$ nm, $g = 130$ nm, $w = 650$ nm, $d = 80$ nm, and $h = 200$ nm. Silicon and sapphire were modeled in the simulations through their refractive index $n_{Si} = 3.47$ and $n_s = 1.74$, respectively. In the theoretical analysis the sapphire substrate was treated as a semi-infinite medium.

The theoretical analysis consisted in full-wave and eigenvalue simulations using the finite-element method implemented in the commercial software Comsol Multiphysics. In all cases, only the MS unit cell was simulated by applying Floquet periodic boundary conditions at the lateral walls of the computational domain. As the focus was on normal wave incidence, the transverse components of the wavevector were set to zero ($k_x = k_y = 0$).

Fig. 2(a) shows the calculated full-wave transmittance spectra in the vicinity of the target qBIC resonance for various values of d_x, evidencing the reduction of the resonance linewidth for decreasing values of d_x. The transmittance spectra were fitted to the following Fano formula

$$T_{Fano}(\omega_n) = |t_D|^2 \frac{(F\gamma_n + \omega_n - 1)^2}{(\omega_n - 1)^2 + \gamma_n^2}, \quad (1)$$

where $\omega_n = \omega/\omega_{res}$ is the normalized angular frequency, $\omega_{res} = 2\pi c_0/\lambda_{res}$, λ_{res} being the resonant wavelength, c_0 the speed of light in free space, F the Fano asymmetry parameter and γ_n the damping rate through which the Q-factor can be directly calculated as $Q = 1/2\gamma_n$. In all cases, excellent fitting was achieved, as demonstrated in the indicative case of $d_x = 100$ nm shown in the inset of Fig. 2(a).

Moreover, an eigenfrequency analysis was performed, aiming to complement the full-wave/Fano-fitting results. The analysis provided the resonant wavelength and Q-factor of the qBIC resonance as a function of d_x by calculating the corresponding complex qBIC eigenfrequency $\tilde{\omega}$ ($Q = \Re\{\tilde{\omega}\}/2\Im\{\tilde{\omega}\}$). Fig. 2(b) and (c) shows the dependence on d_x of the resonant wavelength and radiative Q-factor, respectively, demonstrating very good agreement. As expected for symmetry-protected qBIC resonances, the Q-factor increases dramatically for small degrees of asymmetry and asymptotically tends to infinity due to vanishing radiation losses, under the assumption of lossless materials. In the small perturbation regime, the Q-factor follows the inverse quadratic law with respect to the asymmetry parameter d_x, shown as the dashed line in Fig. 2(c), which is a characteristic property of symmetry-protected, non-diffracting qBIC metasurfaces [23]. For larger values of d_x the Q-factor drops faster as the asymmetric unit cell cannot longer be considered as a weak perturbation [24]. The resonant wavelength increases for higher values of d_x, as part of the air slot is substituted by high-index silicon in the volume of the unit cell.

The eigenfrequency analysis also provides an efficient tool to inspect the electric field profile of the BIC mode, which is shown in Fig. 3(a) for the symmetric structure ($d_x = 0$), calculated at the midplane of the silicon layer ($z = h/2$) and at the $x = p/4$ cross-section plane. The field is mostly concentrated inside the CSR segments, resembling slot modes in slotted silicon nanowire waveguides. The arrows show the direction of the electric field (in logarithmic scale) and they reveal the electric quadrupole nature of the resonant BIC mode. Close inspection of the field profile around the field minima positions reveals only slight differences among the two regions occupied by the silicon bridge and those in the slots. The modal eigenfield profile shows the same symmetry as the structure (C_{2v}), although the perturbation with respect to C_{4v} is small, since the silicon bridges occupy regions with low field intensity. This particular aspect of the slotted mode field profile implies that the introduction of the asymmetry parameter d_x is expected to only slightly perturb the resonant field, thus allowing for larger values of d_x to achieve a given degree of coupling to the resonant mode.

The symmetry properties of such SP-BIC modes can be analyzed by means of the symmetry adapted linear combination (SALC) method [25, 26]. The irreducible representation (IRREP) of this mode is B_2 in the group C_{4v} and reduces to A_2 in C_{2v}. However, in both cases the incident field **E** belongs to a different IRREP (E and B_2 for C_{4v} and
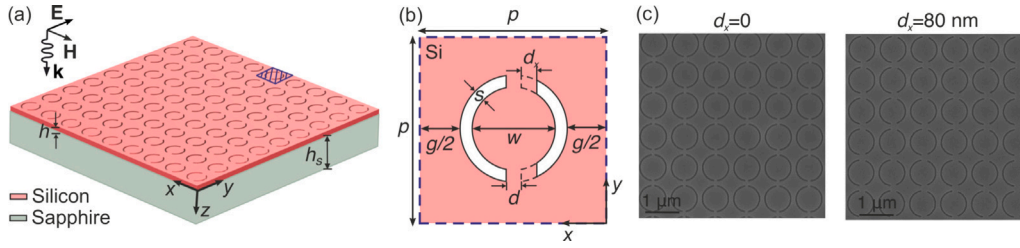
Fig. 1. (a) Bird's eye view of the investigated silicon-on-sapphire metasurface. The metasurface is composed of split-ring slot segments etched in a $h = 200$ nm silicon layer grown on a $h_s = 430$ μm sapphire substrate. (b) Geometry of the metasurface unit cell. The symmetry is broken by shortening the arc length of one of the two slots via the asymmetry parameter d_x. (c) Scanning electron microscope images of two fabricated samples corresponding to the symmetric metasurface ($d_x = 0$) and one with broken symmetry ($d_x = 80$ nm).
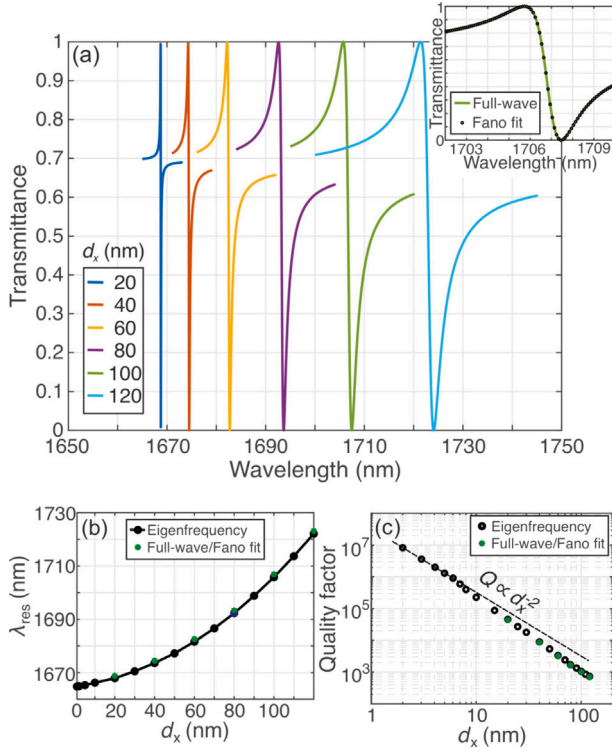

Fig. 2. (a) Full-wave calculated transmittance spectra of the metasurface around the qBIC resonance for various values of d_x. The spectra were fitted to the Fano formula of Eq. (1) with excellent fitting, as evidenced in the inset for $d_x = 100$ nm. (b) Variation of the resonant wavelength and (c) Q-factor of the qBIC mode calculated by eigenfrequency analysis and by the corresponding Fano parameters of the fitted full-wave spectra.
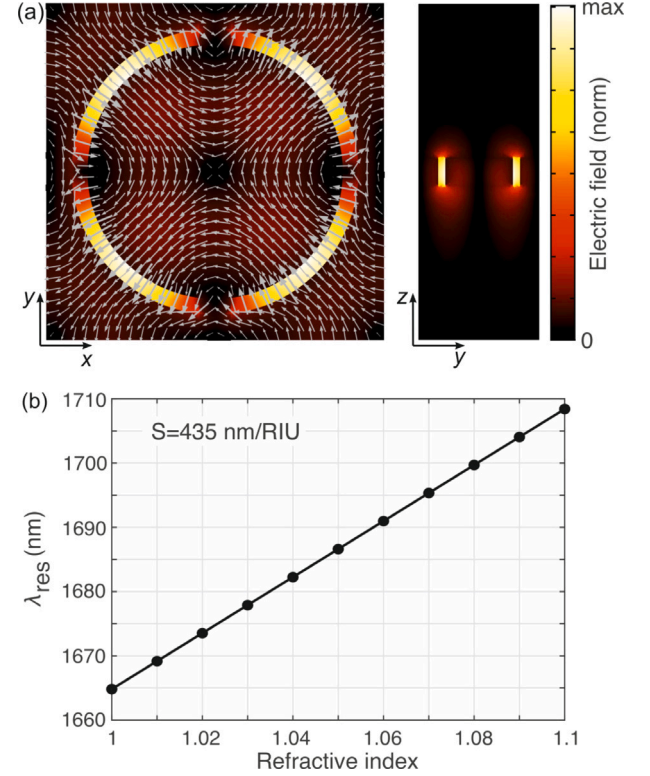

Fig. 3. (a) Electric field profile of the BIC eigenmode calculated at the silicon layer midplane of the metasurface and the $x = p/4$ plane, demonstrating the silicon-slot nature of the mode. The arrows (in log scale) show the direction of the electric field and reveal an electric-quadrupole type mode. (b) Variation of the resonant wavelength calculated by eigenfrequency analysis as a function of the superstratum refractive index. The sensitivity value is $S = 435$ nm/RIU and it is linear in the investigated interval.

C_{2v}, respectively) and hence the mode cannot be excited. Reduction to C_s symmetry by introducing $d_x \neq 0$ degenerates the BIC mode IRREP to B, which coincides with that of the field $\mathbf{E}_y$, thus enabling polarization-selective excitation as a qBIC resonance.

The silicon-slot character of the qBIC mode leads to strong interaction of the resonant field with the material occupying the slots. This property can be directly exploited in refractometric sensing by filling the slots with the analyte material. To provide an estimate of the sensitivity of such a sensing platform, defined as $S = \Delta\lambda_{res}/\Delta n_a$, where n_a is the analyte refractive index, we have calculated $\lambda_{res}(n_a)$ employing eigenfrequency analysis for the symmetric MS. The variation of n_a was from 1 to 1.1, which corresponds to the scenario of gas sensing. Fig. 3(b) demonstrates a high value of sensitivity $S = 435$ nm/RIU with an almost perfectly linear profile, a highly desirable trait in sensing applications. The high sensitivity can be, in principle, combined with very high Q-factor values, thus leading to a figure of merit (FoM= QS/λ_{res}) orders of magnitude higher than, for instance, sensors based on plasmonic architectures, which suffer from ohmic

damping losses [27]. In the context of gas refractometry, it is remarked that the variation of the refractive index n_g of standard gases (N$_2$, O$_2$, H$_2$, CO$_2$, CH$_4$, He) lies in the interval $1 < n_g < 1.001$ [28]. Given the abovementioned sensitivity values, the proposed gas sensor would need a spectral resolution in the order of few tens of picometers to discern among various gases. In a real system, the sensor resolution is limited by amplitude noise, thermal fluctuations and the spectral limitation of the detector [29]. Regarding the later, high-resolution optical spectrum analyzers (OSA) offer sub-pm resolution and, hence, standard deviation values [30]. Temperature stabilization can result also in sub-pm standard deviation. The standard deviation of the spectral variation due to amplitude noise can be estimated as $\sigma \simeq \Delta\lambda/(4.5\,\mathrm{SNR}^{0.25})$, where $\Delta\lambda$ and SNR are the resonance linewidth and signal-to-noise-ratio (in linear units), respectively [29]. Considering the conservative value of SNR=60 dB and the Q-factors experimentally measured for the investigated qBIC metasurface (ranging from 500 to 725, details in Section 3), the resonance linewidth is $\Delta\lambda \simeq 3$ nm and the calculated

Table 1

Comparative table of the properties of experimentally demonstrated dielectric metasurface refractometric sensors.

Year	Structure	S [nm/RIU]	Q	FoM	Ref.
2017	SOI photonic crystal slab	94	12000	735	[31]
2018	Si_3N_4 photonic crystal slab	178	2000	445	[32]
2018	SOI nanodisks	720	270	120	[33]
2019	Si_3N_4 guided-mode metasurface	235.2	600	12.3	[34]
2020	Si hollow nanocuboids	161.5	728	78	[35]
2020	TiO_2 nanobars	80.6	852	80.6	[36]
2021	SOI tilted Si nanoellipsoids	788	170	90	[37]
2021	Si crescent-shaped nanocylinders	326	120	52	[38]
2021	Si asymmetric nanoellipsoids	305	179	68	[39]
2021	nanoholes in a-SiO_x film	140	450	94	[40]
2022	Si tilted nanobars	608	102	46	[41]
2022	Si slotted rings	435	725	189	this work[a]

[a]Estimation based on the calculated sensitivity and maximum measured Q-factor.

sensor resolution, established as 3σ of the noise in the system, is in the order of 60 pm, which is compatible with operation as a gas sensor. Significant margins of improvement exist in terms of increasing both the sensitivity and the Q-factor, as it will be thoroughly discussed.

Dielectric metasurface refractometric sensors offer direct integration with microfluidic setups, e.g., polydimethylsiloxane (PDMS) chambers, and free-space coupling for simple read-out, hence they have been intensively researched following various approaches, such as qBIC, bright, or guided-mode resonances. Table 1 summarizes the recent progress in the field by providing the key performance indicators of bulk refractometric sensors, namely S, Q-factor, and FoM. The calculated S for the investigated qBIC metasurface sensor, as well its FoM, as estimated based on the highest measured value $Q = 725$, favorably compare to most of the reported cases, although a direct comparison is not fully consistent as the sensors reported in Table 1 target mostly biosensing applications with analyte refractive indices ~ 1.3. Furthermore, the geometry of the silicon-slot metasurface has not been optimized in terms of the maximum sensitivity. For instance, just by replacing sapphire with standard silica as the substrate, simulations showed that the sensitivity increases to 518 nm ($\lambda_{res} = 1598.6$ nm to 1650.4 nm for $n_a = 1$ to 1.1), thanks to the lower refractive index of silica.

3. Experimental results

The fabrication was carried out in the nanofabrication facilities at SiPhotonIC ApS. The investigated devices were fabricated on a silicon-on-sapphire platform with a 200 nm thick silicon layer epitaxially grown on a 430-μm sapphire substrate. The nanoslots were defined by EBL using CSAR e-beam resist and the JBX-9500FSZ 100 kV E-Beam Writer. After EBL, the STS ICP Advanced Silicon Etcher (ASE) was applied to etch the silicon based on the Bosch etching process, which includes an etching phase with SF_6 and O_2 that alternates with a passivation phase with C_4F_8 for each etching cycle. The gas flow, chamber pressure, platen and coil RF powers were tuned to achieve a vertical etching profile, with almost complete etching of the silicon layer down to the sapphire substrate. After etching, the residual e-beam resist was removed by oxygen plasma cleaning. The dimensions of all metasurface samples, which correspond to different d_x values, were 0.3×0.3 mm^2. Typical SEM images of the surface of two fabricated samples ($d_x = 0$ and 80 nm), are shown in Fig. 1(b). In addition, a high-resolution SEM image showing the details of two adjacent slots of the $d_x = 0$ nm sample is provided in Fig. 4(a). It is observed that the slot width is not constant, but it exhibits a small variation from the nominal value $s = 40$ nm, as it will be discussed later in detail. Fig. 4(b) shows a SEM image of the vertical cross-section profile of the $d_x = 80$ nm sample, taken after processing the sample with focused ion-beam (FIB) milling. The slots are almost fully etched, down to a few nanometers from the interface between the silicon layer and the substrate.
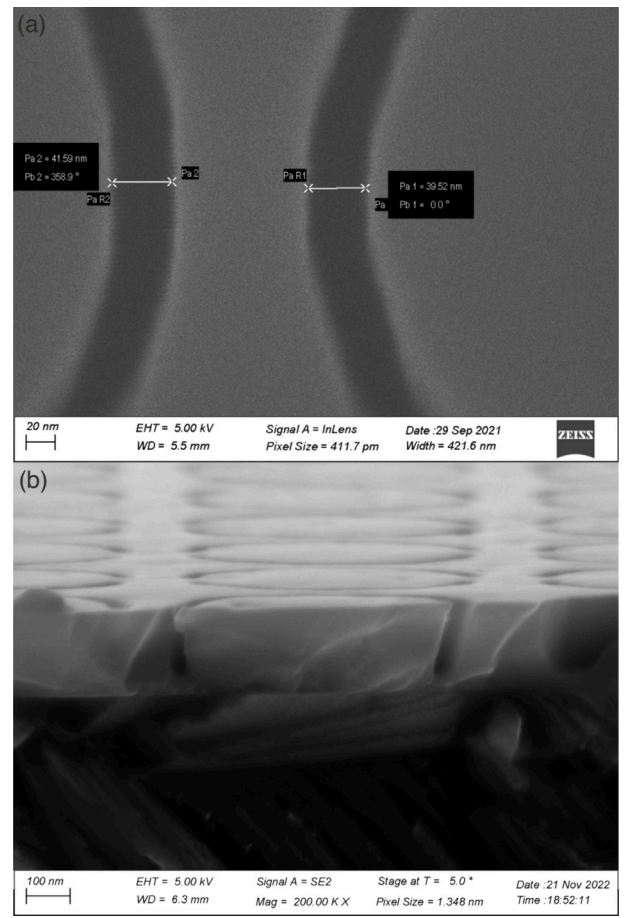

Fig. 4. (a) High-resolution SEM image of the $d_x = 0$ nm sample showing the details of two adjacent slots etched in the silicon layer. (b) SEM image of the vertical cross-section of the $d_x = 80$ nm sample taken after FIB processing.

The transmittance of the various samples was measured under normal incidence of a polarized light beam using a Fourier-transform spectrometer (Bruker IFS66) with a spectral resolution of 0.25 pm (1 cm^{-1}). The light beam from the spectrometer was focused on the sample surface with an Al off-axis parabolic mirror to a spot-size diameter of 100 μm, with an angular spread of ± 0.5 deg. A liquid-nitrogen-cooled InSb photodiode was used as the detector.

Fig. 5 provides a direct comparison of the measured transmittance spectra for samples with varying degree of asymmetry. The ripple observed in all spectra stems from FP oscillations in the sapphire substrate, whose free spectral range $\Delta\lambda_{FP} \simeq 1.92$ nm is consistent with the FP formula $\Delta\lambda_{FP} \simeq \lambda_0^2/(2n_s h_s)$. The qBIC resonance is clearly visible for d_x down to 40 nm, whereas for lower values it is masked by the FP oscillation as well as by resonance damping. The resonant wavelength of the qBIC mode exhibits the expected blue-shift trend for lower d_x.

In order to estimate the qBIC resonance Q-factors, the measured transmittance spectra were fitted to

$$T(\omega_n) = A(\omega_n) + F(\omega_n), \tag{2}$$

where $A(\omega_n)$ is the Airy function that describes the background Fabry–Perot interference in the sapphire substrate [42] and $F(\omega_n)$ is the extended Fano formula [43]

$$F(\omega_n) = \eta_{rad}T_{Fano}(\omega_n) - \beta\frac{\eta_{rad}\eta_{abs}}{1 + \left(\frac{\omega_n-1}{\gamma_n}\right)^2} + \eta_{abs}\left|t_D\right|^2, \tag{3}$$

where β is the intensity of the resonant transmittance at ω_{res} and η_{rad}, η_{abs} are the radiation and absorption probabilities, respectively, of the
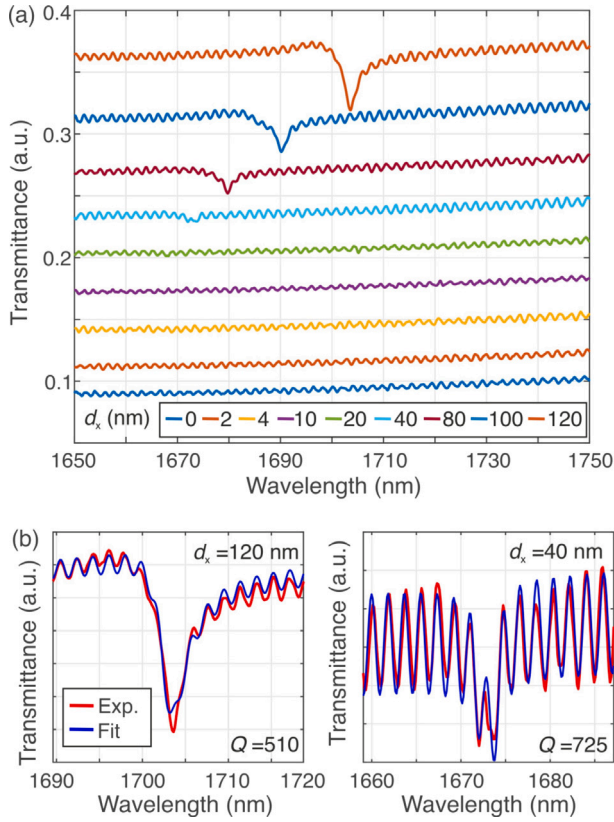
Fig. 5. (a) Experimentally measured transmittance spectra for the fabricated metasurface samples. The qBIC resonant is evident for higher values of d_x. The ripples are due to the Fabry–Perot effect in the sapphire substrate. (b) The fit of the $d_x = 120$ nm and $d_x = 40$ nm spectra to the transmittance formula of Eq. (2).

Fig. 6. (a) Variation of the qBIC resonant wavelength λ_{res} as a function of d_x and the slot width $s = s_0 - \Delta s$, where $s_0 = 40$ nm. (b) Angular dispersion of the qBIC mode for the symmetric metasurface.

Table 2
Comparative table of experimentally measured Q-factor values in near-infrared silicon-based qBIC metasurfaces.

Year	Structure	Q-factor	λ_{res} [nm]	Ref.
2017	square hole array	1011	1300	[44]
2018	asymmetric nanodisks	1946	1490	[45]
2019	photonic crystal slab	490000	1568	[46]
2019	truncated nanocuboids	18511	1550	[47]
2019	asymmetric nanodisks	128	1345	[48]
2019	asymmetric nanobars	175	1450	[24]
2020	square hole array	850	1278	[49]
2021	truncated nanocuboids	8911	1315	[50]
2021	asymmetric nanobars	1500	1510	[51]
2021	photonic crystal slab	7300[a]	1550	[52]
2021	tilted nanoellipsoids	2000	1570	[53]
2021	truncated nanocuboids	3534	1548	[54]
2022	nanodisks	600	1400	[55]
2022	tilted nanobars	130	1350	[41]
2022	silicon slotted rings	725	1673	this work

[a]Limited by measurement resolution.

localized qBIC mode ($\eta_{rad} = 1 - \eta_{abs}$). Fig. 5(b) shows the comparison between the measured spectrum for $d_x = 120$ nm and the fitted Fano function, which is capable of resolving the linewidth of the qBIC resonance. It is stressed that Eq. (3) serves as a mathematical tool to quantify the measured Q-factors and does not provide the complete picture of the involved physics that lead to resonance broadening, as it will be discussed shortly after.

The fitted Q-factors range from $Q = 510$ for $d_x = 120$ mn to $Q = 725$ for $d_x = 40$ nm. For $d_x \leq 20$ nm, namely smaller than the e-beam spotsize, the qBIC was not detectable in the transmittance spectra due to complete quenching. The measured Q values are of the same
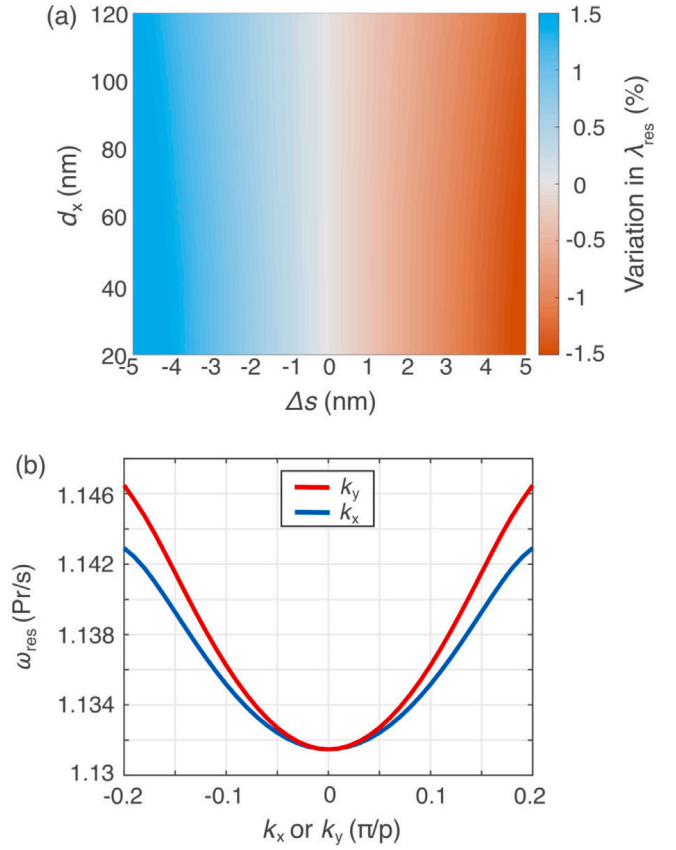
order of magnitude compared to most experimental demonstrations of silicon-based qBIC metasurfaces (although not based on silicon-slot resonances), with the notable exceptions of the truncated nanocuboid metasurface paradigm [47,50,54] and the concept of merging BIC in photonic crystal slab structures [46,52]. Table 2 summarizes recent progress in the field and places the results of this study in the context.

The measured Q values are significantly lower than the theoretical ones due to resonance damping. The latter may stem from various factors [56], of which one of the most critical is often statistical variations of the geometrical features of the fabricated metasurfaces [57]. We have conducted an investigation by post-processing SEM images such as in Fig. 1(b) and Fig. 4 (more examples shown in Section 1 of the Supplementary Information) on the slot width s, as this was found to be the most sensitive parameter in terms of defining the qBIC resonance wavelength λ_{res}. A quasi-normal statistical distribution was observed with a standard deviation of $\sigma_s = 2.41$ nm (see Section 2 of the Supplementary Information). Fig. 6(a) shows simulation results on the dependence of λ_{res} as a function of d_x and the slot width, where Δs is the variation from the nominal value of $s_0 = 40$ nm, namely $s = s_0 + \Delta s$. It is demonstrated that for the indicative case $\Delta s = \pm \sigma_s$ the qBIC resonant wavelength varies in the order of $\Delta \lambda_{res}/\lambda_{res} \simeq 1.5\%$, almost independently of d_x. Although an accurate estimate of the induced resonance broadening, as for instance described in Ref. [57], is beyond the scope of this work, the level of variation in λ_{res} considering the measured statistical distribution accounts for the measured Q-values, which are limited below 1000.

Other factors that may contribute to the observed resonance damping are: (i) scattering losses caused by etching-induced surface roughness of silicon at the slot walls, (ii) the finite lateral extent of the metasurface, and (iii) the small angular spread of $\theta_b = 0.5°$ of the probing

light beam. The latter two factors cause resonance broadening owing to the fact that they lead to the excitation of the qBIC resonant mode at off-Γ k-vector points, which have different resonant wavelengths due to the dispersion of the qBIC mode. This spectral broadening (as previously observed [42]) limits the maximum observable Q-factor according to the following constrain:

$$Q \leq \frac{\omega_{\text{res}}}{b \Delta k^2}, \tag{4}$$

where Δk is the wavevector spread and $b = \frac{1}{2} \frac{d^2 \omega_{\text{res}}}{dk^2}|_{k=0}$ [26]. In the case of a non-collimated probe beam with an angular spread θ_{b}, the wavevector spread equals $\Delta k_{\text{b}} = k_{\text{res}} \sin \theta_{\text{b}}$, where $k_{\text{res}} = 2\pi/\lambda_{\text{res}}$. In the case of a finite-size metasurface, the k-spread stems from the perturbation of the resonant mode in the finite structure, which leads to a wavenumber fluctuation $\Delta k_{\text{fs}} \simeq 2\pi/L$ off the Γ point in the quantized k-space, where L is the lateral size of the metasurface [58,59]. Since the fabricated samples have $L = 0.3$ mm, $\lambda_{\text{res}} \simeq 1.665$ nm, and $\theta_{\text{b}} = 0.5°$, it follows that $\Delta k_{\text{fs}} < \Delta k_{\text{b}}$, hence the Q-factor is in this case limited by the beam angular spread.

To estimate the maximum measurable Q-factor, the dispersion $\omega_{\text{res}}(k)$ of the investigated qBIC around the Γ-point is calculated for the symmetric structure and for variations of both k_x and k_y. The results, shown in Fig. 6(b), demonstrating a parabolic-type dispersion, which is larger for variations of the k_y wavevector component. The corresponding parameter b is estimated at $b_y \simeq 40$ m^2/s and the maximum Q-factor is $Q_{\text{max}} \simeq 26000$, which is more than one order of magnitude higher than the measured values. Hence, we attribute the observed resonance damping primarily to fabrication limitations, both in terms of geometrical feature definition/etching profile and their statistical variation over the metasurface area, most notably that of the slot width. Nevertheless, the results clearly demonstrate the scope of this work, which was the experimental verification of the investigated silicon-slot qBIC resonant mode in the proposed dielectric metasurfaces.

4. Conclusions

To sum up, this work provides a theoretical and experimental investigation of a silicon dielectric metasurface designed to support a slot-like qBIC in the near IR. Thanks to the qBIC nature and intense field confinement in the metasurface slots, the resonant mode provides both high sensitivity and Q-factors by controlling the degree of asymmetry in the design of the unit cell. The main properties of the proposed qBIC mode were experimentally verified by measuring the transmittance of samples with varying degree of asymmetry, fabricated by EBL on a silicon-on-sapphire substrate. The measured Q-factors showed notable resonance damping stemming from various factors that are discussed in detail. The proof-of-concept demonstration of this silicon-slot qBIC resonant mode in dielectric metasurfaces can stimulate the engineering of metasurface-based devices for refractometry or other applications demanding strong field confinement in nanometric resonant volumes.

CRediT authorship contribution statement

J.F. Algorri: Conceptualization, Methodology, Software, Writing – original draft, Writing – review & editing. **F. Dell'Olio:** Conceptualization, Writing – original draft, Writing – review & editing, Project administration, Funding acquisition. **Y. Ding:** Investigation, Resources, Writing – review & editing. **F. Labbé:** Investigation, Writing – review & editing. **V. Dmitriev:** Formal analysis, Writing – review & editing. **J.M. López-Higuera:** Writing – review & editing, Supervision, Funding acquisition. **J.M. Sánchez-Pena:** Writing – review & editing, Funding acquisition. **L.C. Andreani:** Software, Formal analysis, Resources, Data curation, Writing – review & editing, Visualization, Supervision. **M. Galli:** Investigation, Resources, Writing – review & editing. **D.C. Zografopoulos:** Conceptualization, Methodology, Software, Formal analysis, Data curation, Writing – original draft, Writing – review & editing, Visualization, Supervision.

Declaration of competing interest

The authors declare that they have no known competing financial interests or personal relationships that could have appeared to influence the work reported in this paper.

Data availability

Data will be made available on request.

Appendix A. Supplementary data

Supplementary material related to this article can be found online at https://doi.org/10.1016/j.optlastec.2023.109199.

References

[1] C.W. Hsu, B. Zhen, A.D. Stone, J.D. Joannopoulos, M. Soljačić, Bound states in the continuum, Nat. Rev. Mater. 1 (2016) 16048.

[2] F. Monticone, A. Alù, Embedded photonic eigenvalues in 3D nanostructures, Phys. Rev. Lett. 112 (2014) 213903.

[3] M.G. Silveirinha, Trapping light in open plasmonic nanostructures, Phys. Rev. A 89 (2014) 023813.

[4] D.C. Marinica, A.G. Borisov, S.V. Shabanov, Bound states in the continuum in photonics, Phys. Rev. Lett. 100 (2008) 183902.

[5] Y. Plotnik, O. Peleg, F. Dreisow, M. Heinrich, S. Nolte, A. Szameit, M. Segev, Experimental observation of optical bound states in the continuum, Phys. Rev. Lett. 107 (2011) 183901.

[6] Z. Sadrieva, K. Frizyuk, M. Petrov, Y. Kivshar, A. Bogdanov, Multipolar origin of bound states in the continuum, Phys. Rev. B 100 (2019) 115303.

[7] S. Joseph, S. Pandey, S. Sarkar, J. Joseph, Bound states in the continuum in resonant nanostructures: an overview of engineered materials for tailored applications, Nanophotonics 10 (2021) 4175–4207.

[8] C.W. Hsu, B. Zhen, J. Lee, S.-L. Chua, S.G. Johnson, J.D. Joannopoulos, M. Soljačić, Observation of trapped light within the radiation continuum, Nature 7457 (2013) 188–191.

[9] Y. Yang, C. Peng, Y. Liang, Z. Li, S. Noda, Analytical perspective for bound states in the continuum in photonic crystal slabs, Phys. Rev. Lett. 113 (2014) 037401.

[10] S. Weimann, Y. Xu, R. Keil, A.E. Miroshnichenko, A. Tünnermann, S. Nolte, A.A. Sukhorukov, A. Szameit, Y.S. Kivshar, Compact surface Fano states embedded in the continuum of waveguide arrays, Phys. Rev. Lett. 111 (2013) 240403.

[11] S.I. Azzam, A.V. Kildishev, Photonic bound states in the continuum: From basics to applications, Adv. Opt. Mater. 9 (2021) 2001469.

[12] F. Monticone, A. Alù, Bound states within the radiation continuum in diffraction gratings and the role of leaky modes, New J. Phys. 19 (2017) 093011.

[13] M. Wu, L. Ding, R.P. Sabatini, L.K. Sagar, G. Bappi, R. Paniagua-Domínguez, E.H. Sargent, A.I. Kuznetsov, Bound state in the continuum in nanoantenna-coupled slab waveguide enables low-threshold quantum-dot lasing, Nano Lett. 21 (2021) 9754–9760.

[14] H.-F. Wang, S.K. Gupta, X.-Y. Zhu, M.-H. Lu, X.-P. Liu, Y.-F. Chen, Bound states in the continuum in a bilayer photonic crystal with TE-TM cross coupling, Phys. Rev. B 98 (2018) 214101.

[15] A.S. Kupriianov, Y. Xu, A. Sayanskiy, V. Dmitriev, Y.S. Kivshar, V.R. Tuz, Metasurface engineering through bound states in the continuum, Phys. Rev. Appl. 12 (2019) 014024.

[16] J.F. Algorri, B. García-Cámara, A. Cuadrado, J.M. Sánchez-Pena, R. Vergaz, Selective dielectric metasurfaces based on directional conditions of silicon nanopillars, Nanomaterials 7 (2017) 177.

[17] M.F. Picardi, A.V. Zayats, F.J. Rodríguez-Fortuño, Janus and Huygens dipoles: Near-field directionality beyond spin-momentum locking, Phys. Rev. Lett. 120 (2018) 117402.

[18] J.F. Algorri, D.C. Zografopoulos, A. Ferraro, B. García-Cámara, R. Vergaz, R. Beccherelli, J.M. Sánchez-Pena, Anapole modes in hollow nanocuboid dielectric metasurfaces for refractometric sensing, Nanomaterials 9 (2019) 30.

[19] V. Dmitriev, D.C. Zografopoulos, S.D.S. Santos, G.F. da Silva Barros, Flat metasurfaces with square supercells of 2×2 dielectric disk quadrumers: tailoring the fine structure of toroidal mode local field, J. Phys. D: Appl. Phys. 55 (2022) 205104.

[20] A.A. Bogdanov, K.L. Koshelev, P.V. Kapitanova, M.V. Rybin, S.A. Gladyshev, Z.F. Sadrieva, K.B. Samusev, Y.S. Kivshar, M.F. Limonov, Bound states in the continuum and Fano resonances in the strong mode coupling regime, Adv. Photonics 1 (2019) 1–12.

[21] J.F. Algorri, F. Dell'Olio, P. Roldán-Varona, L. Rodríguez-Cobo, J.M. López-Higuera, J.M. Sánchez-Pena, D.C. Zografopoulos, Strongly resonant silicon slot metasurfaces with symmetry-protected bound states in the continuum, Opt. Express 29 (2021) 10374–10385.

[22] A.A. Barybin, V.A. Dmitriev (Eds.), Modern Electrodynamics and Coupled-Mode Theory: Application to Guided-Wave Optics, IOS Press, Amsterdam, NY, 2002.

[23] K. Koshelev, S. Lepeshov, M. Liu, A. Bogdanov, Y. Kivshar, Asymmetric metasurfaces with high-Q resonances governed by bound states in the continuum, Phys. Rev. Lett. 121 (2018) 193903.

[24] K. Koshelev, Y. Tang, K. Li, D.-Y. Choi, G. Li, Y. Kivshar, Nonlinear metasurfaces governed by bound states in the continuum, ACS Photonics 6 (2019) 1639–1644.

[25] J.F. Algorri, F. Dell'Olio, P. Roldán-Varona, L. Rodríguez-Cobo, J.-M. López-Higuera, J. Sánchez-Pena, V. Dmitriev, D.C. Zografopoulos, Analogue of electromagnetically induced transparency in square slotted silicon metasurfaces supporting bound states in the continuum, Opt. Express 30 (2022) 4615–4630.

[26] A.C. Overvig, S.C. Malek, M.J. Carter, S. Shrestha, N. Yu, Selection rules for quasibound states in the continuum, Phys. Rev. B 102 (2020) 035434.

[27] D.C. Zografopoulos, V. Dmitriev, Quasi-dark resonances in silicon metasurface for refractometric sensing and tunable notch filtering, J. Lightw. Technol. 39 (2021) 6985–6993.

[28] P.K. Maharana, R. Jha, P. Padhy, On the electric field enhancement and performance of SPR gas sensor based on graphene for visible and near infrared, Sens. Act. B 207 (2015) 117–122.

[29] I.M. White, X. Fan, On the performance quantification of resonant refractive index sensors, Opt. Express 16 (2008) 1020–1028.

[30] APEX Technologies, AP208x high-resolution optical spectrum analyzers. https://www.apex-t.com/high-resolution-optical-spectrum-analyzer-ap208x-series/.

[31] Y. Liu, W. Zhou, Y. Sun, Optical refractive index sensing based on high-Q bound states in the continuum in free-space coupled photonic crystal slabs, Sensors 17 (2017) 1861.

[32] S. Romano, G. Zito, S. Torino, G. Calafiore, E. Penzo, G. Coppola, S. Cabrini, I. Rendina, V. Mocella, Label-free sensing of ultralow-weight molecules with all-dielectric metasurfaces supporting bound states in the continuum, Photon. Res. 6 (2018) 726–733.

[33] Y. Wang, Md. A. Ali, E.K.C. Chow, L. Dong, M. Lu, An optofluidic metasurface for lateral flow-through detection of breast cancer biomarker, Biosens. Bioelectron. 107 (2018) 224–229.

[34] D.U. Yildirim, A. Ghobadi, M.C. Soydan, M. Gokbayrak, A. Toprak, B. Butun, E. Ozbay, Colorimetric and near-absolute polarization-insensitive refractive-index sensing in all-dielectric guided-mode resonance based metasurface, J. Phys. Chem. C 123 (2019) 19125–19134.

[35] P.-A. Jeong, M.-D. Goldflam, S. Campione, J.L. Briscoe, P.P. Vabishchevich, J. Nogan, M.B. Sinclair, T.S. Luk, I. Brener, High quality factor toroidal resonances in dielectric metasurfaces, ACS Photonics 7 (2020) 1699–1707.

[36] Y. Chen, C. Zhao, Y. Zhang, C.-W. Qiu, Integrated molar chiral sensing based on high-Q metasurface, Nano Lett. 20 (2020) 8696–8703.

[37] B. Ma, A. Ouyang, J. Zhong, P.A. Belov, R.K. Sinha, W. Qian, P. Ghosh, Q. Li, All-dielectric metasurface for sensing microcystin-LR, Electronics 10 (2021) 1363.

[38] J. Wang, J. Kühne, T. Karamanos, C. Rockstuhl, S.A. Maier, A. Tittl, All-dielectric crescent metasurface sensor driven by bound states in the continuum, Adv. Func. Mater. 31 (2021) 2104652.

[39] Y. Jahani, E.R. Arvelo, F. Yesilkoy, K. Koshelev, C. Cianciaruso, M. De Palma, Y. Kivshar, H. Altug, Imaging-based spectrometer-less optofluidic biosensors based on dielectric metasurfaces for detecting extracellular vesicles, Nat. Commun. 12 (2021) 3246.

[40] D. Conteduca, I. Barth, G. Pitruzzello, C.P. Reardon, E.-R. Martins, T.F. Krauss, Dielectric nanohole array metasurface for high- resolution near-field sensing and imaging, Nat. Commun. 12 (2021) 3293.

[41] H.-H. Hsiao, Y.-C. Hsu, A.-Y. Liu, J.-C. Hsieh, Y.-H. Lin, Ultrasensitive refractive index sensing based on the quasi-bound states in the continuum of all-dielectric metasurfaces, Adv. Opt. Mater. 10 (2022) 2200812.

[42] M. Galli, D. Bajoni, M. Belotti, F. Paleari, M. Patrini, G. Guizzetti, D. Gerace, M. Agio, L. Andreani, D. Peyrade, Y. Chen, Measurement of photonic mode dispersion and linewidths in silicon-on-insulator photonic crystal slabs, IEEE J. Sel. Areas Commun. 23 (2005) 1402–1410.

[43] J.W. Yoon, R. Magnusson, Fano resonance formula for lossy two-port systems, Opt. Express 21 (2013) 17751–17759.

[44] S. Yuan, X. Qiu, C. Cui, L. Zhu, Y. Wang, Y. Li, J. Song, Q. Huang, J. Xia, Strong photoluminescence enhancement in all-dielectric Fano metasurface with high quality factor, ACS Nano 11 (2017) 10704–10711.

[45] C. Cui, C. Zhou, S. Yuan, X. Qiu, L. Zhu, Y. Wang, Y. Li, J. Song, Q. Huang, Y. Wang, C. Zeng, J. Xia, Multiple Fano resonances in symmetry-breaking silicon metasurface for manipulating light emission, ACS Photonics 5 (2018) 4074–4080.

[46] J. Jin, X. Yin, L. Ni, M. Soljačić, B. Zhen, C. Peng, Topologically enabled ultrahigh-Q guided resonances robust to out-of-plane scattering, Nature 574 (2019) 501–505.

[47] Z. Liu, Y. Xu, Y. Lin, J. Xiang, T. Feng, Q. Cao, J. Li, S. Lan, J. Liu, High-Q quasibound states in the continuum for nonlinear metasurfaces, Phys. Rev. Lett. 123 (2019) 253901.

[48] L. Xu, K.Z. Kamali, L. Huang, M. Rahmani, A. Smirnov, R. Camacho-Morales, Y. Ma, G. Zhang, M. Woolley, D. Neshev, A.E. Miroshnichenko, Dynamic nonlinear image tuning through magnetic dipole quasi-BIC ultrathin resonators, Adv. Sci. 5 (2019) 1802119.

[49] L. Zhu, S. Yuan, C. Zeng, J. Xia, Manipulating photoluminescence of carbon G-center in silicon metasurface with optical bound states in the continuum, Adv. Opt. Mater. 8 (2020) 1901830.

[50] Z. Liu, J. Wang, B. Chen, Y. Wei, W. Liu, J. Liu, Giant enhancement of continuous wave second harmonic generation from few-layer GaSe coupled to high-Q quasi bound states in the continuum, Nano Lett. 21 (2021) 7405–7410.

[51] I.S. Sinev, K. Koshelev, Z. Liu, A. Rudenko, K. Ladutenko, A. Shcherbakov, Z. Sadrieva, M. Baranov, T. Itina, J. Liu, A.A. Bogdanov, Y. Kivshar, Observation of ultrafast self-action effects in quasi-BIC resonant metasurfaces, Nano Lett. 21 (2021) 8848–8855.

[52] M.-S. Hwang, H.-C. Lee, K.-H. Kim, K.-Y. Jeong, S.-H. Kwon, K. Koshelev, Y. Kivshar, H.-G. Park, Ultralow-threshold laser using super-bound states in the continuum, Nat. Commun. 12 (2021) 4135.

[53] S. Yang, C. Hong, Y. Jiang, J.-C. Ndukaife, Nanoparticle trapping in a quasi-BIC system, ACS Photonics 8 (2021) 1961–1971.

[54] C. Fang, Q. Yang, Q. Yuan, X. Gan, J. Zhao, Y. Shao, Y. Liu, G. Han, Y. Hao, High-q resonances governed by the quasi-bound states in the continuum in all-dielectric metasurfaces, Opto-Electron. Adv. 4 (2021) 200030.

[55] G. Yang, S.U. Dev, M.S. Allen, J.W. Allen, H. Harutyunyan, Optical bound states in the continuum enabled by magnetic resonances coupled to a mirror, Nano Lett. 22 (2022) 2001–2008.

[56] D.C. Zografopoulos, O. Tsilipakos, Recent advances in strongly-resonant and gradient all-dielectric metasurfaces, Mater. Adv. (2022) http://dx.doi.org/10.1039/D2MA00910B.

[57] J. Kühne, J. Wang, T. Weber, L. Kühner, S.A. Maier, A. Tittl, Fabrication robustness in BIC metasurfaces, Nanophotonics 10 (2021) 4305–4312.

[58] H.-Y. Ryu, M. Notomi, Y.-H. Lee, Finite-difference time-domain investigation of band-edge resonant modes in finite-size two-dimensional photonic crystal slab, Phys. Rev. B 68 (2003) 045209.

[59] Y. Liang, C. Peng, K. Sakai, S. Iwahashi, S. Noda, Three-dimensional coupled-wave analysis for square-lattice photonic crystal surface emitting lasers with transverse-electric polarization: finite-size effects, Opt. Express 20 (2012) 15945–15961.

Supplementary Information for:

Experimental demonstration of a silicon-slot quasi-bound state in the continuum in near-infrared all-dielectric metasurfaces

J. F. Algorri[a,b,c], F. Dell'Olio[d], Y. Ding[e,f], F. Labbé[f], V. Dmitriev[g], J. M. López-Higuera[a,b,c], J. M. Sánchez-Pena[h], L. C. Andreani[i], M. Galli[i], D. C. Zografopoulos[j,*]

[a]Photonics Engineering Group, University of Cantabria, Santander, 39005, Spain
[b]CIBER-bbn, Instituto de Salud Carlos III, Madrid, 28029, Spain
[c]Instituto de Investigación Sanitaria Valdecilla (IDIVAL), Santander, 39011, Spain
[d]Department of Electrical and Information Engineering, Polytecnic University of Bari, Bari, 70125, Italy
[e]SiPhotonIC ApS, Virum Stationsvej 207, Virum, 2830, Denmark
[f]Department of Electrical and Photonics Engineering, Technical University of Denmark, Ørsteds Plads, Bygning 343, Kongens Lyngby, 2800, Denmark
[g]Electrical Engineering Department, Federal University of Pará, PO Box 8619, Agencia UFPA, Belém, 66075-900, Brazil
[h]Department of Electronic Technology, Carlos III University, Madrid, 28911, Spain
[i]Dipartimento di Fisica, Università di Pavia, Pavia, 27100, Italy
[j]Consiglio Nazionale delle Ricerche, Istituto per la Microelettronica e Microsistemi, Via del fosso del cavaliere 100, Rome, 00133, Italy

*Corresponding author (*Email:* dimitrios.zografopoulos@artov.imm.cnr.it)

1. Additional SEM images

Here we provide an indicative set of SEM images showing various aspects of the fabricated samples. Figures S1(a-c) are high-resolution images, with a sub-nm pixel size, which focus on the details of adjacent slots, taken from the $d_x = 0$, 40, and 80 nm samples. A direct estimation of the slot size is provided, where a deviation in the order of a few nanometers from the nominal value of $s = 40$ nm is observed.

Figures S1(d-f) are SEM images showing a top-surface view, a 35° tilted view, and a vertical cross-section taken indicatively from the $d_x = 80$ nm sample, whereas zoomed versions of those are presented in Fig. S1(g-i).

The investigation of the SEM images, such as Fig. S1(f,i) showed that the slots were etched almost to the bottom of the silicon slab, with a residual non-etched layer of a few nanometers and a near-vertical etching profile.

2. Statistical analysis of the geometry of the fabricated samples

Based on a set of SEM images, such as those shown in Fig. S1, an analysis was performed on the statistical distribution of the slot width s and the total dimension of the silicon bridge, defined as $d_t = d + d_x$, over large surface areas of the samples.

The image processing was performed in Python: first, the SEM images were imported as an array of greyscale tones $T(x, y)$. Then, the slot width was estimated by taking straight lines over the image, calculating the greyscale profiles, and setting a threshold value so as to clearly identify silicon from slotted air regions. A similar process, taking circular lines centered
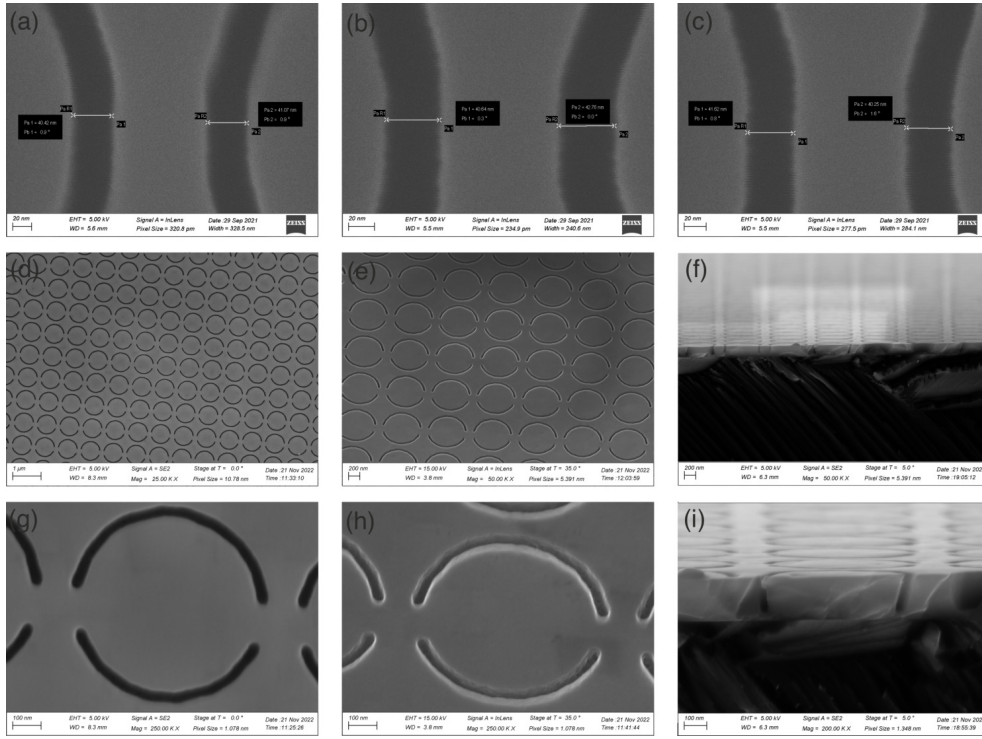
Figure S1: High-resolution SEM images showing the details of adjacent slots for the: (a) $d_x = 0$, (b) $d_x = 40$, and (c) $d_x = 80$ nm samples, respectively. SEM images showing: (d) top-surface view, (e) tilted view at 35°, and (f) vertical cross-section of the $d_x = 80$ nm sample. (g-i) Zoomed versions of the images shown in (d-f).

within the slots and determining the greyscale profiles, was applied to estimate the variations of the total silicon bridge width d_t.

Histograms were produced from the data on the statistical variations of s and d_t, as shown in Fig. S2 for the case study of the $d_x = 80$ nm sample. The average value and standard deviation for the slot width is $s_{av} \simeq 37$ nm and $\sigma_s \simeq 2.4$ nm, respectively. The corresponding values for the bridge width are $d_{t,av} \simeq 147.5$ nm and $\sigma_d \simeq 4.6$ nm. These values demonstrate a good quality of the nanofabrication process, considering that the design value of the slot

Figure S2: Histograms showing the statistical distribution of (a) the slot width s and (b) the bridge width $d_t = d + d_x$ over the surface of the $d_x = 80$ nm sample.

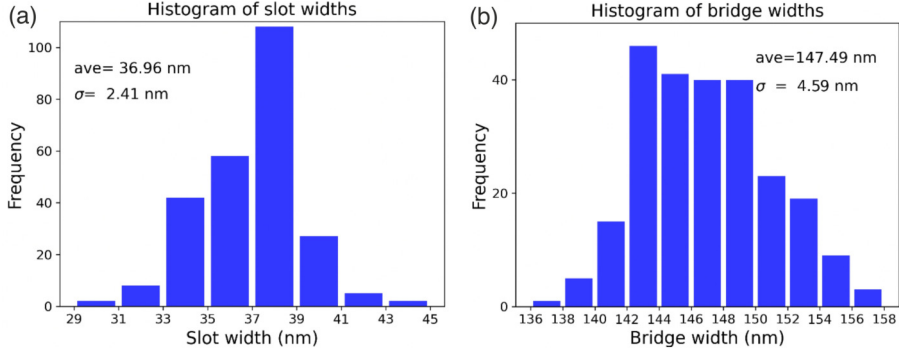³² width is comparable with the size of the electron-beam spot.

³³ In order to provide an assessment of the resulting resonance broadening
³⁴ due to the non-uniformity of the slot width, we have calculated the relative
³⁵ shift of the qBIC resonant wavelength for variations Δs from the nominal
³⁶ value $s_0 = 40$ nm and as a function of d_x. The results are shown in Fig. 6(a)
³⁷ of the main manuscript and they demonstrate that a slot width variation
³⁸ equal to $\pm \sigma_s$ shifts the qBIC resonant wavelength by approximately 1.5%,
³⁹ almost regardless of d_x. In this regard, the corresponding total shift of λ_{res}
⁴⁰ due to the statistical variation of the bridge width $\pm \sigma_d$ is much lower, around
⁴¹ 0.3%. This value was calculated based on the results shown in Fig. 2(b) of
⁴² the main manuscript, for the limit case were the entire variation σ_d is assigned
⁴³ to d_x. Therefore, it is concluded that the variation of the slot width, which in
⁴⁴ relative values is in the order of $\sigma_d / \sigma_{\mathrm{av}} \simeq 6.5\%$, is most likely the dominant
⁴⁵ factor accounting for the observed resonance broadening.

4

Figure S2: Histograms showing the statistical distribution of (a) the slot width s and (b) the bridge width $d_t = d + d_x$ over the surface of the $d_x = 80$ nm sample.

32 width is comparable with the size of the electron-beam spot.

33 In order to provide an assessment of the resulting resonance broadening
34 due to the non-uniformity of the slot width, we have calculated the relative
35 shift of the qBIC resonant wavelength for variations Δs from the nominal
36 value $s_0 = 40$ nm and as a function of d_x. The results are shown in Fig. 6(a)
37 of the main manuscript and they demonstrate that a slot width variation
38 equal to $\pm \sigma_s$ shifts the qBIC resonant wavelength by approximately 1.5%,
39 almost regardless of d_x. In this regard, the corresponding total shift of λ_{res}
40 due to the statistical variation of the bridge width $\pm \sigma_d$ is much lower, around
41 0.3%. This value was calculated based on the results shown in Fig. 2(b) of
42 the main manuscript, for the limit case were the entire variation σ_d is assigned
43 to d_x. Therefore, it is concluded that the variation of the slot width, which in
44 relative values is in the order of $\sigma_d / \sigma_{\mathrm{av}} \simeq 6.5\%$, is most likely the dominant
45 factor accounting for the observed resonance broadening.